Nuclear absorption and emission in the AGN merger NGC 6240: the hard X-ray view

Emanuele Nardini[1]⋆

[1]*INAF – Osservatorio Astrofisico di Arcetri, Largo Enrico Fermi 5, I-50125 Firenze, Italy*

Released Xxxx Xxxxx XX

ABSTRACT

We present the analysis of four *NuSTAR* observations of the luminous infrared galaxy merger NGC 6240, hosting a close pair of highly obscured active galactic nuclei (AGN). Over a period of about two years, the source exhibits hard X-ray variability of the order of 20 per cent, peaking around 20 keV. When the two AGN are resolved with *Chandra*, column densities in the range $N_{\rm H} \sim 1$–2×10^{24} cm^{-2} are estimated for both of them. The exact values are hard to determine, as they appear to depend on aspects that are sometimes overlooked in Compton-thick objects, such as the covering factor of the absorber, iron abundance, and the contamination in the Fe K band from foreground hot-gas emission. Nearly spherical covering and slightly subsolar iron abundance are preferred in this case. While the southern nucleus is suggested to be intrinsically more powerful, as also implied by the mid-IR and 2–10 keV brightness ratios, solutions involving a similar X-ray luminosity of the two AGN cannot be ruled out. The observed variability is rather limited compared to the one revealed by the *Swift*/BAT light curve, and it can be fully explained by changes in the continuum flux from the two AGN, without requiring significant column density variations. NGC 6240 is hereby confirmed to represent a unique opportunity to investigate the X-ray (and broad-band) properties of massive galaxy mergers, which were much more frequent in the early Universe.

Key words: galaxies: active – galaxies: starburst – X-rays: galaxies – galaxies: individual: NGC 6240

1 INTRODUCTION

In the framework of hierarchical structure assembly over cosmic time (e.g. Springel et al. 2005), major mergers are a key phase of galaxy evolution. The existence of close supermassive black hole (SMBH) pairs is therefore inevitable. As the merger advances, the loss of angular momentum from the gas and the subsequent inflows towards the nuclear regions trigger a violent burst of star formation and efficient accretion onto the SMBHs, which are then transformed into active galactic nuclei (AGN). In the local Universe, one of the most impressive objects of this kind is NGC 6240 ($z \simeq 0.0245$; Downes, Solomon & Radford 1993). On its way to entering the ultimate stage of coalescence between two gas-rich spirals (Fosbury & Wall 1979; Fried & Schulz 1983; Wright, Joseph & Meikle 1984), becoming an ultra-luminous infrared galaxy ($L_{\rm IR} > 10^{12} L_{\odot}$) and eventually a passive elliptical (Tacconi et al. 1999; Bush et al. 2008), NGC 6240 is an ideal target to look into many aspects of galaxy evolution at once, including merger dynamics, AGN/starburst interplay, winds and feedback, chemical enrichment. In fact, NGC 6240 has

it all: a distorted optical morphology with long tidal tails (Gerssen et al. 2004) and two nuclei separated by 0.7–0.8 kpc (Max, Canalizo & de Vries 2007), which are likely the remnants of the original galactic bulges (Engel et al. 2010a); a huge ($\sim 10^{10} M_{\odot}$) molecular gas content in the central kpc, peaking between the nuclei and pervaded by turbulence and shocks with different velocity (Iono et al. 2007; Meijerink et al. 2013; Tunnard et al. 2015); a star formation rate of several tens of solar masses per year (Yun & Carilli 2002), thought to drive a starburst superwind that expands into the Hα and soft X-ray emitting circumnuclear nebula (Heckman, Armus & Miley 1987; Lira et al. 2002), possibly extending out to galactic scales (Nardini et al. 2013; Yoshida et al. 2016); and, finally, a pair of buried AGN, one in each nucleus, which can be clearly identified only in the hard X-ray band (2.5–8 keV; Komossa et al. 2003).

As both AGN in NGC 6240 are extremely obscured, only circumstantial evidence of their presence is found at other wavelengths (Gallimore & Beswick 2004; Risaliti et al. 2006; Armus et al. 2006; Hagiwara, Baan & Klöckner 2011). Hence our knowledge of their energy input and of their impact on the system is still disappointingly scant. This largely relies upon the X-ray study, since Iwasawa &

⋆ E-mail: enardini@arcetri.inaf.it

Comastri (1998) detected a prominent Fe K complex on top of a flat 3–10 keV continuum, resembling the spectrum of a typical obscured Seyfert galaxy like NGC 1068, but nearly ten times more luminous. The footprint of the direct AGN emission was revealed soon afterwards by *BeppoSAX* above 10 keV (Vignati et al. 1999). In this work we present the results of four *NuSTAR* observations of NGC 6240 taken over a period of about two years, and discuss their implications on the intrinsic properties of the two AGN and on the nature of their obscuration.

2   OBSERVATIONS AND DATA REDUCTION

NGC 6240 was first observed by *NuSTAR* on 2014 March 30, as part of the satellite's Extragalactic Survey. The results of this observation have been discussed in detail by Puccetti et al. (2016). The source was subsequently targeted on three further occasions during the present monitoring programme, on 2015 April 17, 2015 September 6, and 2016 February 20. All the four data sets were reprocessed with the *NuS-TAR* Data Analysis Software[1] v1.7.1 included in the HEA-SOFT v6.20 release, using the 20170120 version of the calibration files. Cleaned events were obtained with the `nupipeline` task, applying the usual filtering criteria except for the more conservative (*optimized*) treatment of the background in correspondence with the spacecraft passages through the South Atlantic Anomaly. This reduced the good-time interval by about 1–3 ks per Focal Plane Module (A and B) over each of the 2015–2016 observations. Accordingly, the cumulative net exposures are 92.2 ks for FPMA and 91.9 for FPMB (Table 1). Source light curves and spectra were extracted from circular regions with radius of 75 arcsec centred on the target, while the associated background data products were obtained from adjacent regions with radius of 90 arcsec on the same detector.[2] The source counts typically exceed 90 per cent of the total counts in the 3–78 keV band, dominating up to 50–60 keV. The spectra were rebinned in order to oversample the intrinsic energy resolution (400 eV below 40 keV; Harrison et al. 2013) by a factor of 2.5, and further grouped to ensure a significance of at least 5σ per spectral channel.

Seven *XMM–Newton* observations of NGC 6240 were carried out between 2000 September 22 and 2003 August 29, during revolutions 144, 413, 597, 599, 673, 677, and 681 (Boller et al. 2003; Netzer et al. 2005). All of these visits were plagued by strong background flares, so that only a small fraction of the potential exposure is left available after the application of the standard background cuts (28.0 ks for pn, 41.9 ks for MOS1, and 43.2 ks for MOS2; Table 1). The data were reprocessed with the Science Analysis System (SAS) v16.0 and the latest calibration files. Source and background spectra were extracted from circular regions with radii of 30 and 60 arcsec, respectively. Response files were generated with the SAS tasks `rmfgen` and `arfgen`, then the spectra from each detector were combined over all the

[2] The differences between source and background extraction areas were properly taken into account at each step and for each satellite through the BACKSCAL keyword in the file headers.
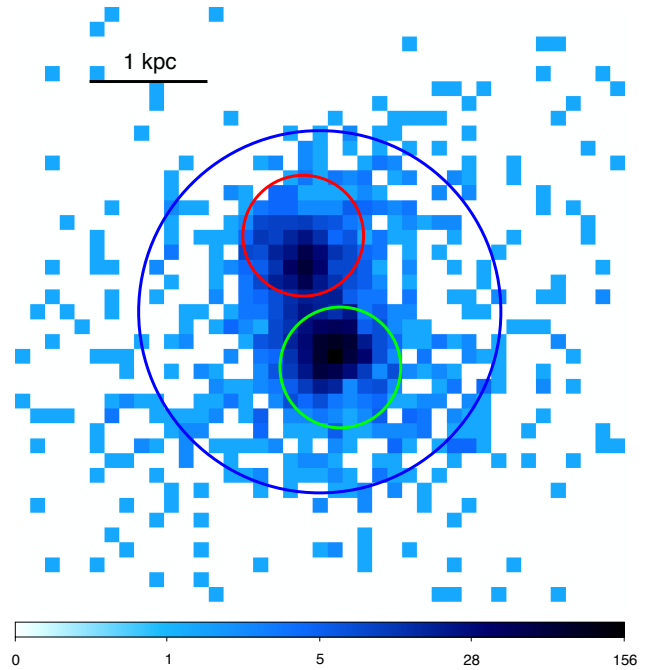

Figure 1. *Chandra* image of the central (10×10 arcsec^2) region of NGC 6240 in the 5–7.5 keV band (rest frame), obtained by combining the ACIS-S observations of 2001 July (ObsID 1590) and 2011 May (ObsID 12713). Subpixel resolution by a factor two is adopted, so one pixel in this figure has a physical size of 126 pc. The regions employed in the spatially resolved spectral analysis are also shown: northern nucleus (red), southern nucleus (green), and diffuse Fe K emission (blue).

epochs with `epicspeccombine`, and grouped to a 5σ significance per bin. After verifying their consistency, the two MOS spectra were further combined into a single one.

NGC 6240 was also observed by *Chandra* with the Advanced CCD Imaging Spectrometer (ACIS) on four times. The observations of 2006 May 11 and 16, however, were taken with the High Energy Transmission Grating (HETG), thus significantly reducing the effective area of ACIS-S. The zeroth-order images were considered here, but they were eventually discarded as their quality is not sufficient to improve the results of the broad-band spectral analysis.[3] The data from the other two *Chandra* observations (performed on 2001 July 29 and 2011 May 31) were reprocessed by running the `chandra_repro` script within the CIAO v4.9 software package, using the Calibration Database (CALDB) version 4.7.3 and following the steps described in Nardini et al. (2013). With respect to the whole galaxy, the size of the regions employed for the spectral extraction is the same as for *XMM–Newton*. Thanks to the exceptional angular resolution afforded by *Chandra*, spectra were also extracted separately for each nucleus and for the central (3-arcsec radius) region that encompasses, besides the nuclei, most of the diffuse emission in the Fe K band (Wang et al. 2014). In the

[3] The total number of net counts in the 0.5–8 keV band collected in the two HETG observations is about one fourth (10500 versus 41300) of those collected without the gratings.

Table 1. Observation log of the X-ray spectra analysed in this work. Net exposures and count rates are listed. $\mathcal{F}_{S/T}$ is the fraction of source to total counts in the reference band. Fluxes are derived from the best-fitting models in Section 3, and are not corrected for cross calibration.

Satellite	Date	Detector	Exposure (s)	Band (keV)	Count Rate (s^{-1})	$\mathcal{F}_{S/T}$ (%)	Flux (erg s^{-1} cm^{-2})
NuSTAR (1)	2014 Mar 30	FPMA	30,860	3–78	0.180±0.003	92.0	5.08×10^{-11}
		FPMB	30,783		0.166±0.003	89.2	5.02×10^{-11}
NuSTAR (2)	2015 Apr 17	FPMA	20,494	3–78	0.207±0.003	93.5	5.63×10^{-11}
		FPMB	20,508		0.193±0.003	91.0	5.75×10^{-11}
NuSTAR (3)	2015 Sep 06	FPMA	20,411	3–78	0.202±0.003	93.7	5.47×10^{-11}
		FPMB	20,203		0.189±0.003	91.0	5.47×10^{-11}
NuSTAR (4)	2016 Feb 20	FPMA	20,421	3–78	0.180±0.003	92.0	4.67×10^{-11}
		FPMB	20,433		0.168±0.003	90.2	4.74×10^{-11}
XMM–Newton	[2000–2003]	pn	27,983	0.5–8	0.484±0.004	97.5	1.98×10^{-12}
		MOS	85,040		0.153±0.001	98.1	2.08×10^{-12}
Chandra	[2001–2011]	ACIS-S	182,053	0.5–8	0.227±0.001	97.1	2.19×10^{-12}

former case, two circles with radius of 1 arcsec were chosen (Fig. 1), with a slight offset from the corresponding peaks of the 5–7.5 keV surface brightness in order to minimize the contamination from the nearby companion. Given the relative positions, count rates, and encircled energy fractions at 6.4 keV, this is estimated to be less than 2 and 4 per cent for the southern nucleus and the northern one, respectively. All the spectra were combined and grouped with the same criteria adopted above.

The key details of all the data sets analysed in this work are provided in Table 1. The fitting packages XSPEC[4] v12.9.1 and SHERPA[5] v4.9 were used in the analysis. Unless otherwise stated, uncertainties are given at the 1σ confidence level for count rates and fluxes, and at the 90 per cent level ($\Delta\chi^2 = 2.71$) for the single parameter of interest in the spectral models. The latest values of the concordance cosmological parameters ($H_0 = 67.7$ km s^{-1} Mpc^{-1}, $\Omega_m = 0.31$, $\Omega_\Lambda = 0.69$; Planck Collaboration XIII 2016) are assumed throughout, based on which the luminosity distance and angular scale of NGC 6240 are 111 Mpc and 512 pc $arcsec^{-1}$.

3 ANALYSIS AND DISCUSSION

3.1 Hard X-ray light curves

Above 10 keV, NGC 6240 is characterized by remarkable variability, as revealed by the *Swift*/BAT hard X-ray survey (Baumgartner et al. 2013). The 70-month 14–195 keV light curve, binned to periods of five months to match the time span between the 2015–2016 *NuSTAR* observations, is shown in Fig. 2. The flux of the source is highly erratic, as it can either remain stable or vary by up to a factor of two over about a year. A fit with a constant returns a statistic of $\chi^2/\nu = 37.8/13$, and can be rejected with a significance of 3.6σ. The long-term hard X-ray variability and its dependence on energy of more than one hundred AGN selected from the 58-month *Swift*/BAT catalogue have been recently studied by Soldi et al. (2014). In that work, NGC 6240 stands

out as one of the most intriguing objects. While the amplitude of the variability in the 14–24 and 35–100 keV bands is strongly correlated over the entire sample, in NGC 6240 the overall intensity changes (e.g. Fig. 2) appear to be almost exclusively due to the lower energy band.

Since the column density towards the nuclear regions of NGC 6240 lies most likely in the range 1–2×10^{24} cm^{-2} (Vignati et al. 1999; Ikebe et al. 2000; Puccetti et al. 2016), that is, around or just above the conventional threshold for Compton thickness,[6] any change in N_H of the order of a few $\times 10^{23}$ cm^{-2} could be readily detectable at 5–10 keV. The historical spectra, however, are virtually consistent with each other over this range, within the cross calibration uncertainties between the various X-ray observatories (although it should be noted that the quality of the individual spectra, other than the 2011 *Chandra* ACIS-S one, is generally too low to derive robust constraints in this sense). The peak of the variability around 20 keV therefore remains somewhat puzzling. With its imaging capabilities that allow for the first time an accurate subtraction of the hard X-ray background, *NuSTAR* can finally shed new light on the striking behaviour of NGC 6240 at high energies.

The 3–78 keV light curves from the four *NuSTAR* observations, normalized to the average count rate, are plotted in Fig. 3 (top panel). Absolute values are provided in Table 2, together with the results obtained by fitting each sequence and the overall trend with a constant. A time bin of 5800 s has been adopted, roughly corresponding to the satellite's orbital period. The final bin of the first sequence was discarded because of its low (~ 10 per cent) fractional exposure. Over the entire *NuSTAR* band, the source is clearly variable between the different epochs. In the brightest state (2015 April) the count rate is about 15 per cent higher than in the faintest one (2016 February). Even though this range is not as large as that exhibited in the whole *Swift*/BAT survey, the statistical significance of the variability increases to the 7.5σ level. Conversely, the short-term fluctuations noticed within the single observations can be in the first instance

[6] This is defined as $N_H > (x\sigma_T)^{-1} \sim 1.23 \times 10^{24}$ cm^{-2}, where x is the mean number of electrons per hydrogen atom and σ_T is the Thomson cross section (e.g. Murphy & Yaqoob 2009).
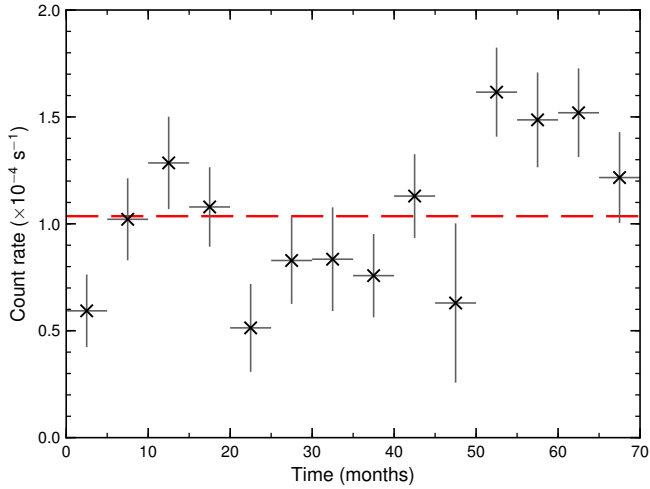
Figure 2. Hard X-ray (14–195 keV) light curve of NGC 6240 from the *Swift*/BAT 70-month survey (2004 December to 2010 September) in time bins of five months, commensurate with the separation between the last three *NuSTAR* observations. The source is clearly variable around the average (red dashed line), and significant flux changes can occur on time-scales of about one year.

neglected, as the null-hypothesis probability of the constant fits is always > 0.05 (Table 2).

Light curves were also extracted separately in the soft (3–10 keV) and hard (10–40 keV) *NuSTAR* bands, and the hardness ratio of the latter over the former has been computed (Fig. 3). This brings out the energy dependence of the above variability, which is again confirmed to be more pronounced around 20 keV. Indeed, the 3–10 keV count rate is broadly consistent with being constant ($\chi^2/\nu = 41.7/33$), and the global intensity changes between the observations are mostly driven by the 10–40 keV band ($\chi^2/\nu = 138/33$). In turn, this implies that some spectral variations are in place, most likely associated with the direct continuum level (see below). The 10–40/3–10 keV hardness ratio bears some interesting indications as well. In spite of 3–78 keV count rates that differ by up to ~ 10 per cent, the first three sequences have almost identical hardness ratios, while the last sequence is not only the faintest, but also the softest (Table 2). The occurrence of states with similar (different) flux but different (similar) spectral shape suggests that the high-energy variability of NGC 6240 might have a complex origin, possibly involving a contribution from both nuclei.

3.2   Average *NuSTAR* spectrum

While there is tentative evidence that the fourth observation caught NGC 6240 in a 'softer' state, the hardness ratio is formally consistent with a constant value ($\langle HR \rangle \simeq 2.05$; $\chi^2/\nu = 37.8/33$), i.e. with no evolution with time. The limited extent of any spectral variability then allows us to combine all the data from the four epochs, and to take advantage of the very high quality of the resultant *NuSTAR* spectrum (adding up to a total exposure of ~ 184 ks between FPMA and FPMB) to derive some preliminary information on the properties of the obscuring medium. The soft X-ray emission is probed through the *XMM–Newton* (pn and MOS)
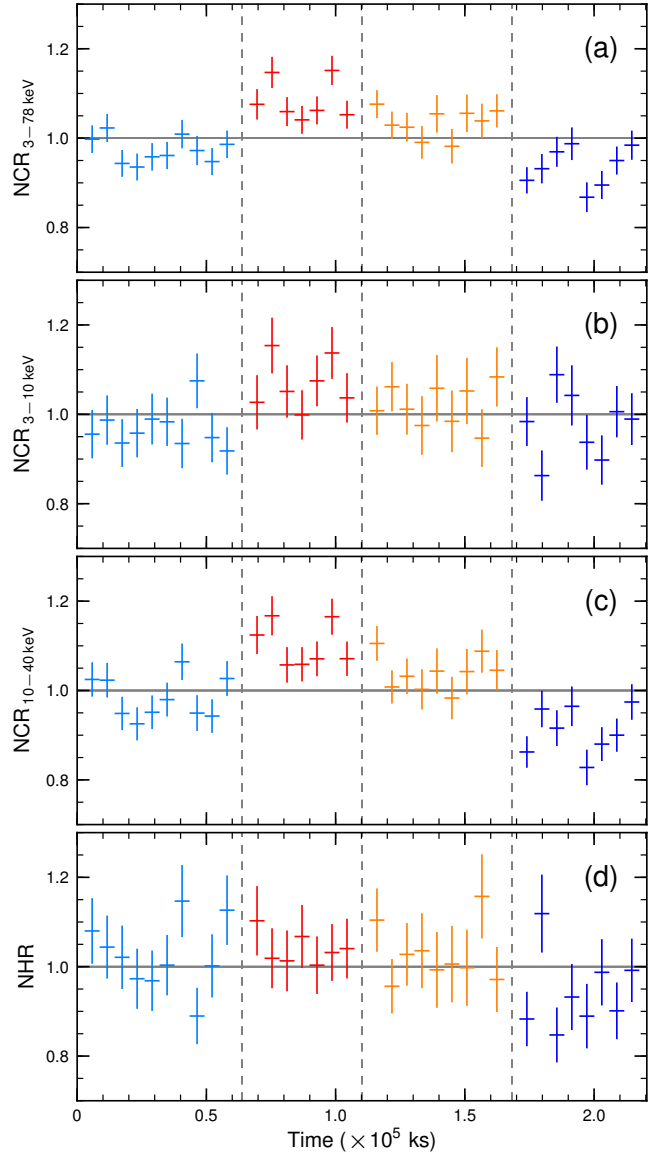

Figure 3. From top to bottom: normalized count rates in the (a) 3–78, (b) 3–10, (c) 10–40 keV bands, and (d) normalized 10–40/3–10 keV hardness ratio for the four *NuSTAR* observations. The background-subtracted light curves from both modules were added together, after the standard corrections for dead time, PSF, and vignetting losses. The horizontal scale portrays the total elapsed time, with the gaps between the observations removed.

and *Chandra* (ACIS-S) spectra, which also provide a better energy resolution in the Fe K band and a benchmark against variability below 10 keV. For ease of comparison, the *XMM–Newton* and *Chandra* spectra were fitted over the common range of 0.5–8 keV, outside of which the effective area of the MOS and ACIS-S detectors rapidly drops. The individual *NuSTAR* spectra from FPMA and FPMB were analysed in the 3–78 keV band.

Thanks to the vast knowledge on this system accumulated with the previous X-ray studies, here we can directly move to a physically motivated picture of the thermal, diffuse emission and of the obscured, nuclear compo-

Table 2. Average values of the 3–78, 3–10, 10–40 keV net count rates (from both FPMA and FPMB) and of the 10–40/3–10 keV hardness ratio for each *NuSTAR* observation, with fit statistic and null-hypothesis probability relative to a constant model.

Observation	2014 Mar	2015 Apr	2015 Sep	2016 Feb	All
$\langle \mathrm{CR}_{3-78\,\mathrm{keV}} \rangle$ (s^{-1})	0.543±0.005	0.604±0.007	0.578±0.007	0.521±0.006	0.558±0.003
χ^2/ν	8.2/9	11.5/6	6.2/8	12.3/7	132/33
Probability	0.512	0.074	0.629	0.091	8.7×10^{-14}
$\langle \mathrm{CR}_{3-10\,\mathrm{keV}} \rangle$ (s^{-1})	0.175±0.003	0.193±0.004	0.185±0.004	0.176±0.004	0.181±0.002
χ^2/ν	5.2/9	5.8/6	4.0/8	10.9/7	41.7/33
Probability	0.817	0.450	0.853	0.143	0.142
$\langle \mathrm{CR}_{10-40\,\mathrm{keV}} \rangle$ (s^{-1})	0.368±0.005	0.412±0.006	0.389±0.005	0.340±0.005	0.375±0.003
χ^2/ν	13.3/9	8.7/6	6.7/8	12.3/7	138/33
Probability	0.150	0.190	0.566	0.091	8.0×10^{-15}
$\langle \mathrm{HR}\frac{10-40\,\mathrm{keV}}{3-10\,\mathrm{keV}} \rangle$	2.087±0.046	2.129±0.053	2.096±0.053	1.908±0.050	2.054±0.025
χ^2/ν	10.5/9	1.4/6	5.3/8	9.0/7	37.8/33
Probability	0.308	0.967	0.722	0.254	0.258

nents. The contribution from collisionally ionized gas with at least three different temperatures has been identified in NGC 6240 (Boller et al. 2003). The gas becomes gradually hotter (and more obscured) as one moves towards the centre, from the cold ($kT \sim 0.6$–0.7 keV) halo detected out to scales of about 100 kpc (Nardini et al. 2013), through the warm ($kT \sim 1$–1.5 keV) butterfly-shaped circumnuclear nebula (Lira et al. 2002), to the shock-heated ($kT \sim 5$–6 keV) environment around and between the nuclei (Wang et al. 2014). With this in mind, the initial spectral model has been defined as follows within xspec:

Model $\mathcal{A}$ = `constant[1]`×`phabs[2]`×(`vmekal[3]` + `zphabs[4]`×`mekal[5]` + `zphabs[6]`×`pshock[7]` + `MYTZ[8]`×`zpowerlw[9]` + `constant[10]`×`MYTS[11]` + `constant[12]`×`MYTL[13]` + `zphabs[14]`×`zpowerlw[15]`),

where `vmekal[3]`, `mekal[5]`, and `pshock[7]` represent the thermal emission from the cold, warm, and hot/shocked plasma, respectively. Abundances of iron and α-elements were allowed to vary in the first component, while solar values (from Anders & Grevesse 1989) were assumed in the other two, which are also affected by foreground absorption (`zphabs[4,6]`), presumably associated with the cold halo itself and/or with the prominent galactic dust lanes (e.g. Max et al. 2005). Compton-thick obscuration and reprocessing of the intrinsic nuclear continuum (`zpowerlw[9]`) were implemented with the MYTorus model (Murphy & Yaqoob 2009), which self-consistently computes the line-of-sight attenuation (MYTZ`[8]`), the scattered continuum (MYTS`[11]`), and the fluorescent emission lines (MYTL`[13]`) from a toroidal absorber with circular cross section and half-opening angle of 60°. The `constant[10,12]` factors adjust the relative weights of the three components, and were initially fixed to 1 (as per the standard 'coupled' configuration; Yaqoob 2012). Given the geometry of MYTorus, a fraction of the direct continuum (`zpowerlw[15]`) can be scattered into the line of sight by optically thin ionized gas in the polar regions,[7] before being possibly absorbed as well (`zphabs[14]`). The

Galactic column density (`phabs[2]`) was set to 4.87×10^{20} cm^{-2} (Kalberla et al. 2005), while `constant[1]` accounts for the cross normalization between the spectra from different detectors, compared to FPMA.

When applied to the *XMM–Newton*, *Chandra*, and average *NuSTAR* spectra, Model $\mathcal{A}$ gives a fairly good fit statistic ($\chi^2/\nu \simeq 1482/1310$). The equatorial column density of the torus is 1.3×10^{24} cm^{-2}, and its inclination angle is 87°. The direct continuum dominates at all energies over the scattered one. Yet this model is not acceptable, due to the presence of clear residuals in the 6–10 keV range. These take the shape of a modest excess, to compensate for which the shock component tends to a much higher temperature than previously reported, $kT = 9.1^{+2.7}_{-1.4}$ keV. Moreover, the strength of the Fe I and Fe XXV lines is not perfectly reproduced. Such a defective outcome is not particularly surprising, given the rigidity of the basic MYTorus configuration as adopted in Model $\mathcal{A}$. These assumptions can be relaxed by 'decoupling' the three MYTorus tables to various degrees (see Yaqoob 2012 for an extensive review). For instance, the relative weights `[10,12]` can be allowed to vary to introduce the effects of time delays between the direct and the reprocessed emission, and the column densities along the line of sight and outside of it can be different. More complex set-ups mimic a clumpy medium. However, none of these solutions works here. Nor does the inclusion in the model of a second nucleus, by doubling the components `[8]` to `[13]`. The improvement is always marginal, leaving a $\chi^2_\nu > 1.12$. The actual shortcomings with Model $\mathcal{A}$ must then reside in one of the features of MYTorus that cannot be circumvented through an ad-hoc decoupling, and specifically the fixed abundances and the global covering factor. Within MYTorus, it is not trivial to obtain a covering factor much larger than the native $\Omega/4\pi = 0.5$, and also the assumption of solar abundances (especially for iron) can have a substantial impact when the data quality is very high.

Thanks to the growing interest in the properties of the Compton-thick AGN population, in the last years several other models have been presented that accurately describe absorption, scattering, and fluorescence in an $N_\mathrm{H} > 10^{24}$ cm^{-2} medium (e.g. Ikeda, Awaki & Terashima 2009; Brightman & Nandra 2011; Liu & Li 2014). Among these, the only

---

[7] This is referred to as 'reflected continuum' in the following, in order to avoid confusion with the scattered component from the cold, Compton-thick material.

geometry that can help us overcome the aforementioned lim-
itations of `MYTorus` is the uniform distribution of matter over
the entire solid angle ($\Omega/4\pi = 1$) of Brightman & Nandra
(2011), whose spectral counterpart is dubbed for simplicity
as `sphere` from now on. In fact, a further advantage of this
model is that iron and total (i.e. common to all the other ele-
ments) abundances are variable. On the other hand, the vari-
ous contributions from transmission, scattering, and fluores-
cence cannot be separated. Thus in Model $\mathcal{B}$ the former com-
ponents [8] to [13] were replaced by a single `sphere` spec-
tral table. The absorbed reflected power law was retained, as
this barely compromises the physical and geometrical self-
consistency of this picture (see also LaMassa et al. 2014,
and below). With abundances frozen to solar, it turns out
that Model $\mathcal{B}$ ($\chi^2/\nu \simeq 1508/1311$) is even worse than Model
$\mathcal{A}$, as the Compton shoulder of the neutral Fe Kα line (e.g.
Yaqoob & Murphy 2011) is slightly overestimated and adds
to the previous residuals. Quite interestingly, the shock tem-
perature is now pushed to the small value of $kT = 3.2^{+0.7}_{-0.4}$
keV, due to the increased amount of scattering into the line
of sight. A complete covering thus appears to be not nec-
essarily involved, justifying some reflection of the intrinsic
continuum that leaks along the clear directions.

As a further step, iron abundance was allowed to vary.
This eventually delivers a very good fit ($\chi^2/\nu \simeq 1358/1310$)
with no significant residuals (Fig. 4). A sensible temperature
of $kT \sim 5\,(\pm 1)$ keV is recovered for the shocked plasma,
while the properties of the cold gas phase are in good agree-
ment with those of the extended soft X-ray halo (Nardini et
al. 2013). Temperature and obscuration ($N_{\rm H} \sim 10^{22}$ cm^{-2})
of the warm component are consistent with those found by
Puccetti et al. (2016), who used a similar model for the
diffuse thermal emission. The best-fitting `sphere` parame-
ters, however, are somewhat unexpected. The column den-
sity and the power-law photon index (see Table 3) are the
same previously obtained with Model $\mathcal{A}$, but the intensity
of the primary continuum is nearly twice as low. A higher
covering factor naturally implies a larger contribution from
scattering, hence the same hard X-ray flux can be produced
by a fainter source. The direct and scattered components
cannot be distinguished from each other within `sphere`, so
their relative importance cannot be immediately quantified.
This notwithstanding, the drop in the continuum intensity
is possibly too large, also given the subsolar iron abundance
($Z_{\rm Fe} \simeq 0.7$) required to achieve a good fit.

The toroidal version of the Brightman & Nandra (2011)
models has been claimed to overestimate the strength of the
reprocessed (scattered plus fluorescent) emission (see Liu
& Li 2015). To verify if this is could be the case also for
the `sphere` component employed in Model $\mathcal{B}$, we switched
to `plcabs` (Yaqoob 1997), which is based on the same as-
sumptions (an isotropic source located at the centre of a
uniform, spherical distribution of matter) and still allows
for variable iron abundance. As `plcabs` does not account
for line fluorescence,[8] two `zgauss` profiles were added in the
new Model $\mathcal{C}$ for the Fe I Kα and Kβ. Moreover, the non-
relativistic approximations become less accurate above 20
keV (see Yaqoob 1997 for details). Keeping in mind that the

---

[8] It does include, instead, continuum scattering into the line of
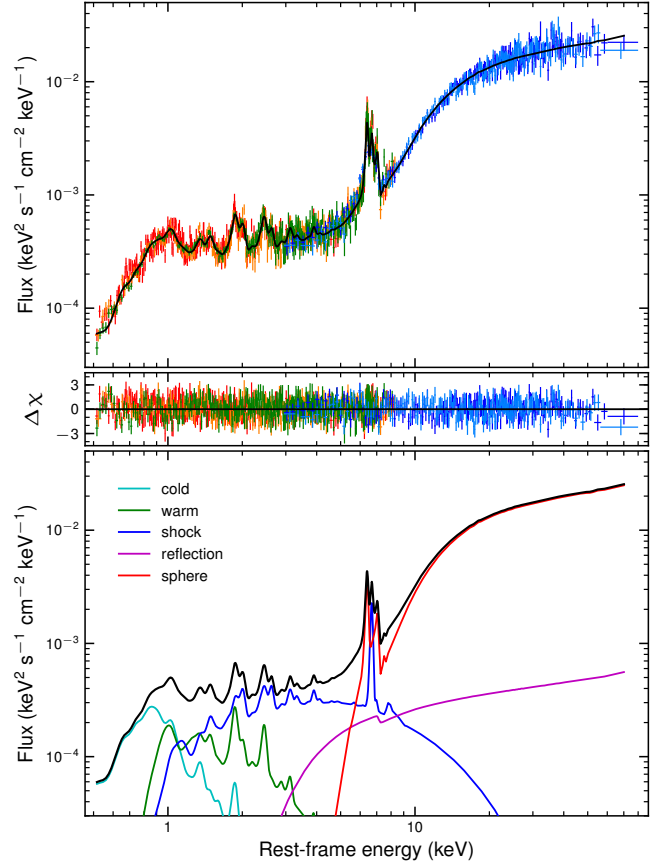sight, so that any additional such component is not required.

Figure 4. Top panel: average *XMM–Newton* (red for pn, orange
for MOS), *Chandra* (green), and *NuSTAR* spectra (light and deep
blue for FPMA and FPMB) of NGC 6240, corrected for cross nor-
malization. Best-fitting Model $\mathcal{B}$ is superimposed (black curve).
Mid panel: residuals in units of σ. Bottom panel: contribution
of the different spectral components, convolved with the *Chandra*
ACIS-S response up to 8 keV, and with the *NuSTAR* one beyond.

---

output of both models should be treated with some caution,
`plcabs` provides nonetheless a direct, meaningful compari-
son with `sphere`. The maximum number of scatterings and
the critical albedo were set to 10 and 0.1, respectively. On
statistical grounds, the use of `plcabs` is fully equivalent to
that of `sphere`, with $\chi^2/\nu \simeq 1352/1306$ and all the param-
eters of the thermal emission that are perfectly matched
between the two models (Table 3). Also the properties of
the reflected continuum are in excellent agreement. In both
cases the scattering fraction is ~ 2–3 per cent, as usually
found in obscured AGN (Noguchi et al. 2010), and the fore-
ground absorption is of the order of $\sim 10^{23}$ cm^{-2}, a typical
obscuration for the central regions of NGC 6240 (Iono et al.
2007).

All of the other quantities associated with the nuclear
component are moderately different. The continuum inten-
sity is increased (close to and consistent with the one inferred
from `MYTorus`), although the photon index is now steeper
($\Gamma \simeq 1.8$ versus 1.7) and the column density is larger by
about 20 per cent. Subsolar iron abundance ($Z_{\rm Fe} \simeq 0.8$) is
preferred in Model $\mathcal{C}$ too, but a solar value cannot be con-
clusively rejected ($\chi^2/\nu \simeq 1360/1307$ for $Z_{\rm Fe} \equiv 1$). Based

Table 3. Best-fitting parameters for Model $\mathcal{B}$ and Model $\mathcal{C}$ (see text for details), applied to the average *XMM–Newton*, *Chandra*, and *NuSTAR* spectra. Galactic absorption is frozen at 4.87×10^{20} cm^{-2}. Abundances are taken to be solar when not specified. Continuum normalizations (K) are computed at 1 keV. EM $= \int n_e n_{\mathrm{H}} \mathrm{d}V$ (where n_e and n_{H} are the electron and hydrogen densities) is the emission measure of the gas. τ_{ion} is the ionization time-scale (see Smith & Hughes 2010). (f) and (t) denote frozen and tied parameters, respectively. The following cross normalization factors were obtained with respect to FPMA: 0.85 ± 0.03 (pn), 0.89 ± 0.03 (MOS), 0.94 ± 0.03 (ACIS-S), and 1.01 ± 0.02 (FPMB).

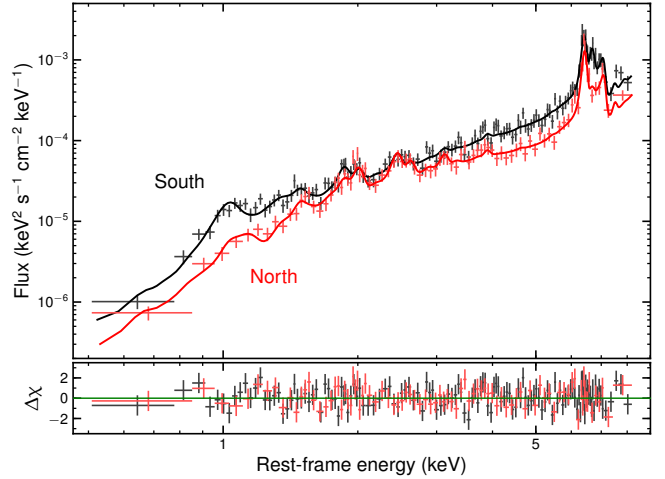| Component Parameter	Model $\mathcal{B}$	Model $\mathcal{C}$
`vmekal` (cold thermal emission)		
kT (keV)	$0.56^{+0.02}_{-0.04}$	$0.56^{+0.02}_{-0.04}$
Z_α (solar)	$0.40^{+0.13}_{-0.09}$	$0.40^{+0.13}_{-0.10}$
Z_{Fe} (solar)	$0.19^{+0.04}_{-0.03}$	$0.19^{+0.05}_{-0.03}$
EM (10^{63} cm^{-3})	54^{+8}_{-9}	53^{+9}_{-8}
`mekal` (warm thermal emission)		
N_{H} (10^{22} cm^{-2})	0.95 ± 0.04	0.95 ± 0.04
kT (keV)	$0.84^{+0.04}_{-0.05}$	0.84 ± 0.04
EM (10^{63} cm^{-3})	119^{+18}_{-16}	119 ± 17
`pshock` (hot thermal emission)		
N_{H} (10^{22} cm^{-2})	0.95(t)	0.95(t)
kT (keV)	$5.1^{+1.1}_{-0.8}$	$5.0^{+1.1}_{-0.8}$
τ_{ion} (10^{11} s cm^{-3})	$5.0^{+1.6}_{-1.2}$	$5.2^{+1.9}_{-1.2}$
EM (10^{63} cm^{-3})	108 ± 9	108 ± 9
`sphere`/`plcabs` (nuclear emission)		
Γ	$1.72^{+0.04}_{-0.06}$	1.82 ± 0.05
N_{H} (10^{22} cm^{-2})	129^{+5}_{-6}	156^{+19}_{-9}
Z_{Fe} (solar)	0.72 ± 0.03	$0.79^{+0.10}_{-0.17}$
K (10^{-2} s^{-1} cm^{-2} keV^{-1})	$0.68^{+0.11}_{-0.12}$	$1.07^{+0.22}_{-0.16}$
`2 zgauss` (fluorescent lines)		
E_1 (keV)	–	$6.391^{+0.006}_{-0.007}$
A_1 (10^{-5} s^{-1} cm^{-2})	–	1.46 ± 0.11
E_2 (keV)	–	$7.017^{+0.035}_{-0.017}$
A_2 (10^{-5} s^{-1} cm^{-2})	–	0.22 ± 0.08
`zpowerlw` (reflected continuum)		
N_{H} (10^{22} cm^{-2})	12 ± 4	15^{+8}_{-4}
Γ	1.72(t)	1.82(t)
K (10^{-4} s^{-1} cm^{-2} keV^{-1})	$1.65^{+0.43}_{-0.41}$	$2.52^{+1.17}_{-0.59}$
χ^2/ν	1357.5/1310	1352.0/1306
Probability	0.176	0.183

Figure 5. Resolved *Chandra* spectra of the southern (black) and northern (red) nucleus of NGC 6240, with best-fitting models and relative residuals (in units of σ). Even the simple visual inspection reveals that all of the thermal components are inherently clumpy, and that their temperature and obscuration is locally variable. Note that some additional Ni Kα emission at 7.47 keV might be present in both nuclei.

computational settings and does not treat fluorescence in a self-consistent way.

3.3 The 'double-nucleus' issue

Differently from other bright, heavily obscured AGN with very high-quality *NuSTAR* spectra that show significant hard X-ray variability (e.g. NGC 4945, Puccetti et al. 2014; NGC 1068, Marinucci et al. 2016; Mrk 3, Guainazzi et al. 2016), the interpretation of NGC 6240 is further complicated by its 'double-nucleus' nature. None of the previous models can be regarded as an adequate representation of the actual X-ray illumination and reprocessing pattern in NGC 6240, although the inclusion of a second source is not statistically required. A first attempt to assess the contribution to the hard X-ray emission from each nucleus was made by Puccetti et al. (2016), by fitting the spatially resolved *Chandra* spectra and extrapolating to higher energies. Here we revisit this approach in the light of the indications of the time-averaged analysis above. The spectra of the two AGN are shown in Fig. 5, and their visual inspection is already highly informative. The northern nucleus is known to be fainter, not only in the X-rays but also in the near- and mid-infrared (Risaliti et al. 2006; Asmus et al. 2014; Mori et al. 2014). The north/south brightness ratio is highest at 2–10 keV (about 0.6), and it can be still higher when referred to the AGN only. Indeed, the contamination from the hot plasma is much heavier in the southern nucleus, as revealed by the strength of the Fe XXV emission line, while there is no compelling evidence for such a prominent feature in the northern nucleus. The two spectra are intriguing also at lower energies. Using Fig. 4 as a guidance, a major contribution to the Si XIII–XIV and S XV–XVI complexes at 1.8–2.6 keV is expected from the shocked gas. Their nearly identical intensity might be accidental though, since the presumed dearth of hot matter around the northern nucleus would entail enhanced emission

on these results, it seems plausible that the amount of scattering in `sphere` is indeed overestimated. The discrepancies, however, are not severe. Taking the intrinsic 2–10 keV flux as a reference, `sphere` yields a continuum fainter by 25–30 per cent with respect to `plcabs`, and a smaller difference applies to the column densities. It is not the scope of this work to further investigate the performances of the various models, also because NGC 6240 is not the ideal target for such a study. In the following we thus stick to the use of Model $\mathcal{B}$, as `plcabs` is rather time-consuming with the adopted

Table 4. Best-fitting parameters for the spatially-resolved *Chandra* spectra of the two nuclei, supplemented by the average 15–78 keV *NuSTAR* spectra. The definitions are the same of Table 3.

Component Parameter	North	South
`vmekal` (cold thermal emission)		
kT (keV)	0.56(f)	0.56(f)
Z_α (solar)	0.40(f)	0.40(f)
Z_{Fe} (solar)	0.19(f)	0.19(f)
EM (10^{63} cm^{-3})	< 0.29	0.43±0.15
`mekal` (warm thermal emission)		
N_H (10^{22} cm^{-2})	$3.0^{+1.2}_{-0.7}$	1.2±0.2
kT (keV)	$1.47^{+0.36}_{-0.30}$	$1.07^{+0.20}_{-0.09}$
EM (10^{63} cm^{-3})	37±13	18±7
`pshock` (hot thermal emission)		
N_H (10^{22} cm^{-2})	$0.8^{+0.5}_{-0.4}$	19^{+15}_{-8}
kT (keV)	5.1(f)	5.1(f)
τ_{ion} (10^{11} s cm^{-3})	5.0(f)	5.0(f)
EM (10^{63} cm^{-3})	$3.6^{+5.5}_{-2.6}$	58^{+22}_{-14}
`sphere` (nuclear emission)		
Γ	$1.78^{+0.09}_{-0.04}$	1.78(t)
N_H (10^{22} cm^{-2})	153^{+40}_{-18}	143^{+12}_{-27}
Z_{Fe} (solar)	$0.70^{+0.10}_{-0.08}$	0.70(t)
K (10^{-2} s^{-1} cm^{-2} keV^{-1})	$0.37^{+0.32}_{-0.11}$	$0.49^{+0.13}_{-0.15}$
`zpowerlw` (reflected continuum)		
N_H (10^{22} cm^{-2})	14^{+13}_{-7}	$3.0^{+2.0}_{-1.5}$
Γ	1.78(t)	1.78(t)
K (10^{-4} s^{-1} cm^{-2} keV^{-1})	$0.71^{+0.52}_{-0.24}$	$0.59^{+0.33}_{-0.27}$
χ^2/ν		414.9/432
Probability		0.715

from the warm component. The spectra depart again from each other below 1.5 keV, hinting at differential obscuration and/or inhomogeneity in the cold gas phase.

For these reasons, simply rescaling the emission measures of the thermal components and the normalization of the reflected continuum with respect to the fit of the whole galaxy with Model $\mathcal{B}$ results in a poor outcome ($\chi^2_\nu \sim 1.7$). The column densities of the reflected continuum and of the shocked and warm gas were then allowed to vary independently for each nucleus, alongside the temperature of the latter. Temperature and ionization time-scale of the shock were kept frozen to the best-fitting values of Table 3 because unconstrained,[9] and so were the main parameters of the cold gas apart from its emission measure (Model $\mathcal{B}'$). This leads to a very good fit, yet the uncertainties on both sets of nuclear variables remain extremely large. Following again Fig. 4, it is clear that the AGN-related components become rapidly dominant above 10 keV. The average 15–78 keV *NuSTAR* spectra were then included in the fit to better constrain the primary photon index (tied between the nu-
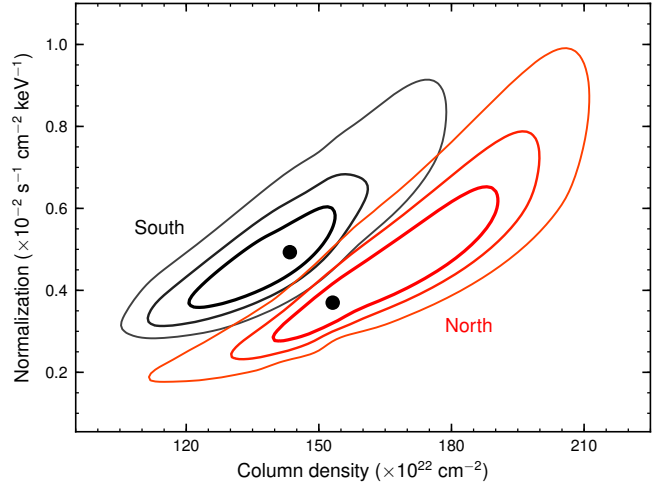

Figure 6. Confidence contours at the 68, 90, and 99 per cent levels in the primary continuum normalization versus column density plane for both nuclei. Despite the mild degeneracy between these quantities, the southern nucleus is generally confirmed to be the brighter and less obscured one. For larger differences between the column density values, however, solutions of equal intrinsic luminosity are still completely allowed.

clei), the intrinsic continuum levels, and the column densities. By construction, this is equivalent to imposing that the sum of the resolved 0.5–8 keV spectra smoothly connects to the total 15–78 keV emission of the source.[10] As a result, the re-adjustment of the best-fitting parameters is negligible in each case, and an excellent fit is obtained ($\chi^2/\nu = 428/434$). The statistic further improves by $\Delta\chi^2/\Delta\nu = -13/-2$ if the redshift of the two `sphere` components (determined in practice by the peak of the Fe Kα feature) is slightly different from the systemic one. This would correspond to a blueshift velocity of -1350^{+660}_{-620} km s^{-1} for the northern nucleus and -590^{+670}_{-600} km s^{-1} for the southern one. These shifts were then accepted, even though they are well within the energy resolution of the spectra and might not have a real physical meaning.

The final fit results (summarized in Table 4) largely support and complement the qualitative picture drawn above. The emission from the shocked gas is about ten times more intense nearby the southern nucleus, and it also more absorbed ($N_H \sim 2 \times 10^{23}$ cm^{-2}). In both cases, the strong features from He- and H-like silicon and sulphur are mostly produced in the warm gas phase, whose temperature and obscuration are subject to local variations. The reflected continuum from the northern nucleus is attenuated by a larger column density, while the opposite trend with similar columns is found for the shock component. Some degeneracy cannot be ruled out, but all the parameters, taken individually, have reasonable values. Indeed, the reflection efficiency of the two nuclei is ~ 1 (south) and 2 per cent (north), and the existence of clumps or filaments with $N_H \sim 10^{22}$–10^{23} cm^{-2} has been firmly established in NGC 6240. The southern AGN still emerges as the more X-ray luminous of the

---

[9] The fit returns $kT \sim 5.5$ keV and $\tau_{ion} \sim 9 \times 10^{11}$ s cm^{-3}, but no useful confidence range can be derived for either quantity.

[10] The same cross normalization factors reported in Table 3 were assumed here between ACIS-S, FPMA, and FPMB.

pair, but by 30 per cent only, i.e. much less than what would be inferred from the mid-IR flux ratios. These are deeply affected by the fierce star formation activity taking place around the southern nucleus (Egami et al. 2006), which is also thought to drive the starburst wind (van der Werf et al. 1993; Ohyama, Yoshida & Takata 2003; Feruglio et al. 2013) that shocks the Fe XXV-emitting gas. Even if the exact X-ray flux and obscuration of the two AGN likely depend upon several factors, among which the local properties of the foreground emitting/absorbing gas, the present results demonstrate that their having the same intrinsic luminosity is a viable solution. Fig. 6 shows the continuum intensity versus column density confidence contours. These are rather elongated in both cases, implying that the two quantities are not entirely independent of one another. In general, however, the greater the column density towards the northern nucleus, the smaller the difference in luminosity between the two AGN.

3.4 Origin of the variability

While the resort to the average *NuSTAR* spectrum has provided new insights into the properties of the single nuclei, the nature of the observed hard X-ray variability remains unclear. Before analysing the *NuSTAR* spectra from the four different epochs, we compared the best-fitting Model $\mathcal{B}'$ for the AGN pair to the broad-band X-ray emission from the whole galaxy. The nuclear contribution inferred in the previous section is consistent with the *NuSTAR* data (extracted over a 75-arcsec radius) down to ~ 12 keV, where a smooth excess (with marginal structures at 6–7 keV) starts rising. Above 3 keV, an excess with the same shape and slightly smaller intensity is found for the *Chandra* spectrum extracted from the central 3-arcsec region, suggesting that this is mostly due to the extended shock component, a significant fraction of which is detected between the nuclei and around them out to several arcsec (Fig. 1; Wang et al. 2014). While the nuclei are responsible for the observed variability, it is impossible to spectrally resolve them within the spatially unresolved spectra, also because of the local differences in the foreground thermal components.

To overcome these limitations and explore how the changes in the nuclear properties (fluxes and/or column densities) affect the overall variability of NGC 6240, we thus made use of the total *Chandra* spectrum, freezing all the parameters of the cold and warm gas phases to the best-fitting values of Table 3. The emission measure and obscuration of the shock component in the neighbourhood of each nucleus, as well as the respective reflected continua, were instead fixed following Table 4. This model is expected to miss a substantial fraction of the shock emission. Indeed, the residuals (shown in Fig. 7) are strongly reminiscent of an absorbed, hot thermal component. On these grounds, we introduced an additional zphabs×pshock contribution with the same temperature and ionization time-scale, while emission measure and obscuration were left free to vary. The model so defined was applied to the *Chandra* and the four pairs of *NuSTAR* spectra. After verifying that the results are not affected and that the cross calibration between FPMA and FPMB is always within 2 per cent (see Table 1), the merged spectra from both modules were used for ease of data handling, and
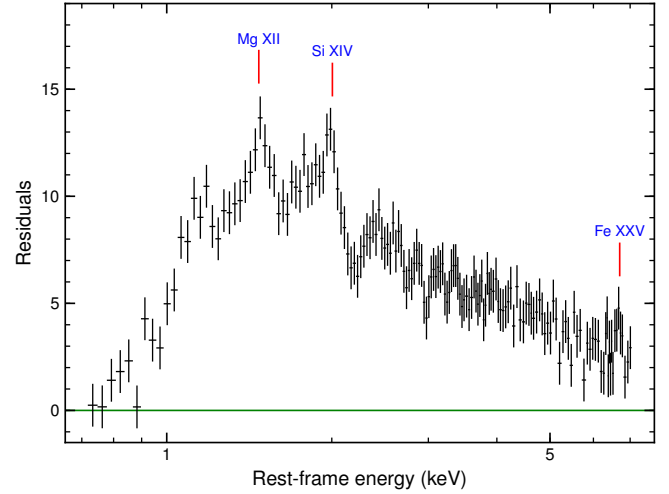

Figure 7. Residuals (in units of σ) in the *Chandra* spectrum of the whole galaxy (rebinned by a factor of two for clarity) with respect to a model consisting of the spatially resolved shock, reflected continuum, and nuclear components plus the large-scale emission from the cold and warm gas phases. The shape closely resembles a thermal spectrum with an absorption cut-off at lower energies. Three major features can be clearly identified from Mg XII, Si XIV, and Fe XXV, which mainly originate from the shock-heated gas (compare with Fig. 4).

the *Chandra* data were tied to those from the first *NuSTAR* observation.

Despite the small number of variables (also photon index and iron abundance are fixed at this stage), the fit is remarkably good, returning a diffuse shock emission with EM $= 95\,(\pm 3) \times 10^{63}$ cm^{-3} absorbed by a screen with $N_{\rm H} \simeq 9 \times 10^{21}$ cm^{-2} (compare with Table 3). As the behaviour of the two AGN cannot be distinguished, we assumed in turn that one of them remains constant, anchoring its flux and column density to the time-averaged values of Table 4. All of the variability is therefore entirely attributed to the other nucleus. In either case, the fit is fully acceptable, with $\chi^2/\nu \simeq 964/948$ when the northern nucleus varies, and $\chi^2/\nu \simeq 963/948$ when the southern one does. Spectra and residuals of the latter fit are plotted in Fig. 8, while the continuum intensity versus column density contours for both nuclei are shown in Fig. 9. Statistically, $N_{\rm H}$ is not required to vary ($\Delta \chi^2/\Delta \nu \simeq 4/3$ in both cases when it is forced to be constant). Quite unpredictably, marginally lower (yet fully consistent) $N_{\rm H}$ values than the ones indicated by the time-averaged analysis seem to be involved. This might be due to a systematic effect hidden in our simplified assumptions. The choice of common parameters (such as the photon index) between the nuclei, for instance, is instrumental in mitigating some degeneracies, but also introduces some complex cross dependencies. Moreover, given the mild spectral variability (Fig. 3, bottom panel), the average *NuSTAR* spectrum might not strictly represent any real state of the source, so the derived quantities should not be taken at face value.

Even considering the uncertainties above, the nuclear columns are very similar (they could differ by as low as $\sim 10^{23}$ cm^{-2}; Table 4), hence the contour patterns of the
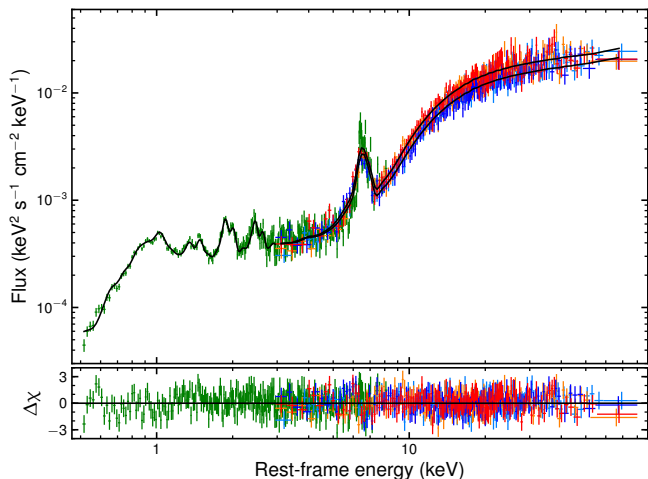
Figure 8. Fit to the *Chandra* and individual *NuSTAR* spectra from the four observations, with the nuclear components disentangled following the spatially-resolved analysis (Table 4) and accounting for the extended shock emission (Fig. 7). The variability is here ascribed to the southern nucleus only. The model divergence above 3 keV between the highest (red, 2015 April) and lowest (blue, 2016 February) *NuSTAR* flux states is shown, with the residuals for all the data sets plotted in the bottom panel.

Figure 9. Confidence contours as in Fig. 6 for a hard X-ray variability entirely due to the southern (left) or northern AGN (right). No changes in the column densities are statistically required. The cross-hair indicates the position of the best-fitting flux and N_H values obtained for that given nucleus from the analysis of the time-averaged *NuSTAR* spectrum, and assumed in the opposite case of non variability (diamond). The colour code for the single observations is the same of Figs. 3 and 8.

two AGN in the X-ray luminosity versus obscuration plane are virtually the same. Then the flux range in Fig. 9 should only set a lower limit to the variability amplitude of each nucleus, which is roughly 40 (south) and 60 per cent (north). Indeed, for similar luminosities a single AGN can dominate the variability only if its central black hole is appreciably less massive than the other, thus accreting at a proportionally larger rate (e.g. Ponti et al. 2012, and references therein). The masses of the two black holes in NGC 6240 are highly uncertain, but they are estimated to have the same order of magnitude, 10^8 to $10^9 M_\odot$, and to lie within a factor of two from each other (Tecza et al. 2000; Engel et al. 2010a; Medling et al. 2015). Both AGN thus likely contribute to the variability. In this view, the tips and dips of the *Swift*/BAT light curve could correspond to periods of simultaneously high and low states of the two AGN, as the relative flux changes would be generally non coherent. Continuum intensity variations as those suggested by Fig. 9 would give rise to visible effects even at 5–10 keV. Hints of this can be tentatively seen in the second *NuSTAR* observation (Figs. 3 and 8). For $N_H < 2 \times 10^{24}$ cm^{-2}, in fact, the direct component is expected to compare with or exceed the scattered one, whose fluctuations are reduced by the superposition of different reprocessing time lags. *Chandra* and *XMM–Newton* might have sampled up to seven states of NGC 6240 (neglecting the observations separated by just a few days), but for various reasons most of them are of little use. Multi-epoch broad-band observations affording high quality data below 10 keV, possibly at high spatial resolution, and catching more extreme spectral states above 10 keV than the ones probed with this campaign, would be therefore needed to achieve a complete X-ray characterization of the two AGN.
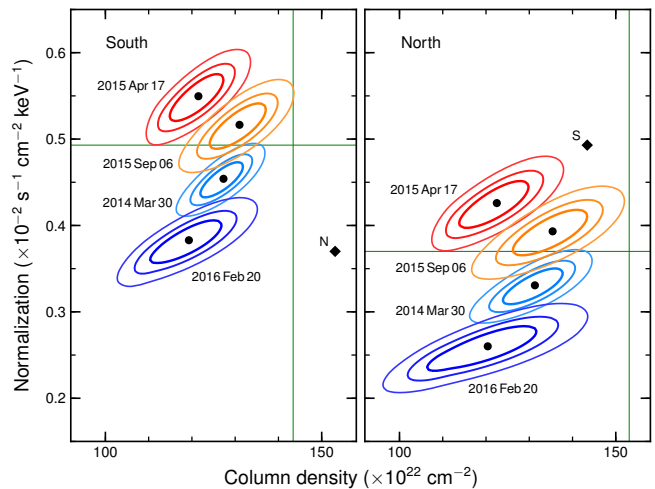
4 SUMMARY AND CONCLUSIONS

In this work, we have reported on the analysis of four *NuSTAR* observations of the galaxy merger NGC 6240, known for hosting a pair of Compton-thick AGN at a separation of less than 1 kpc and a powerful circumnuclear starburst. In the soft X-rays, the spectrum of NGC 6240 is due to gas at different temperatures and physical scales. The highly obscured nuclei emerge above 4 keV, but the emission from shock-heated gas in the starburst superwind is still significant in the Fe K band. Although no clear variability has ever been noticed up to 10 keV, the *Swift*/BAT light curve shows changes by a factor of two, mostly associated with the 14–24 keV energy range (Soldi et al. 2014). The present *NuSTAR* campaign does not probe any extreme flux states, thus providing a combined average spectrum of very good quality. This is best fitted allowing for a nearly spherical covering of the X-ray source and slightly subsolar iron abundance ($Z_{Fe} \simeq 0.7$–0.8) in the absorber.

These results have some important implications for the X-ray study of the local Compton-thick AGN population. Indeed, the most sophisticated and widely used codes of reprocessing by Compton-thick material (e.g. Murphy & Yaqoob 2009; Brightman & Nandra 2011), based on Monte Carlo simulations, were developed before the advent of *NuSTAR*. Now that hard X-ray spectra of unprecedented quality have become available for tens of highly obscured AGN, the theoretical effort is perhaps lagging behind the observations. Especially for the brightest objects, the models might lack some flexibility to explore a broader region of the parameter space. It would be useful, for instance, to understand the impact of the global covering factor and of iron abundance on the measure of the column density, and hence on the estimate of the intrinsic AGN luminosity. This is a crucial step to determine the average properties of the fainter sources

and to assess the contribution of Compton-thick AGN to the cosmic X-ray background (e.g. Gilli, Comastri & Hasinger 2007; Harrison et al. 2016), as metallicity was lower at higher redshift.

The 20 per cent variability observed between the four *NuSTAR* observations can be entirely explained by changes in the direct continuum flux of the two AGN. When their spectra are disentangled below 10 keV thanks to the spatial resolution of *Chandra*, the column densities are quite similar, $N_{\rm H} \sim 1.2$–1.5×10^{24} cm^{-2}, with the northern nucleus that is generally implied to be slightly fainter and more obscured. The larger the difference between the actual foreground columns, the smaller the difference in terms of intrinsic AGN luminosity. The average absorption-corrected 2–10 keV luminosities are about 1.7 and 2.3×10^{43} erg s^{-1} for the northern and the southern nucleus, respectively. We note, however, that the best-fitting values for both $N_{\rm H}$ and the primary X-ray continuum intensity could be somewhat underestimated due to possible systematics in the adopted reprocessing model. The column densities are then likely to fall in the range 1.5–1.9×10^{24} cm^{-2}, for a cumulative 2–10 keV luminosity from the two nuclei of $\sim 6 \times 10^{43}$ erg s^{-1}. Assuming the standard bolometric corrections for obscured AGN (e.g. Lusso et al. 2012; Brightman et al. 2017), this would suggest that the AGN pair contributes to at least 30 per cent of the total energy output of the system.

Our analysis also provides interesting clues on the nature of X-ray absorption in NGC 6240. The comparable column densities towards the two nuclei, the tentative indication of large covering factors, and the lack of evidence for $N_{\rm H}$ changes jointly point to a nuclear obscuration originated by the large amount of gas that is funnelled into the central regions following the tidal perturbations at work during the merger (Springel, Di Matteo & Hernquist 2005). The same gas also serves as a reservoir to efficiently fuel the starburst activity and the enhanced SMBH accretion. Variations of $N_{\rm H}$ are ubiquitous in isolated AGN, but they are typical of a circumnuclear medium that might be clumpy at all scales, like in the revised AGN unification scheme (e.g. Netzer 2015), but preserves an ordered structure overall. The nuclear environment of NGC 6240 is instead highly disturbed and chaotic, and it is reasonable that both AGN are almost completely enshrouded by a nearly uniform shell of dust and gas. Indeed, the incidence of fully covered and Compton-thick AGN is known to increase dramatically among late-stage mergers (Nardini & Risaliti 2011; Ricci et al. 2017). If the bulk of the obscuring matter is supplied by the merger-driven instabilities, column densities of the same order of magnitude for the two nuclei would not be surprising, given the similar gas content and bulge mass of the progenitors.

On the other hand, X-ray absorption might be connected to the excited and high-velocity gas in the nuclear starburst wind, and inflows/outflows in proximity of the two SMBHs could be the cause of the apparent Compton-thickness of the AGN pair. In any case, being one of the most spectacular and complex nearby mergers, caught in a relatively rare evolutionary stage, NGC 6240 stands out as a unique laboratory to study in detail the physics of a prevalent phenomenon of the early Universe, which is the trigger to the most luminous episodes of star formation and nuclear activity (e.g. Engel et al. 2010b; Treister et al. 2012).

REFERENCES

Anders E., Grevesse N., 1989, GeCoA, 53, 197
Armus L., et al., 2006, ApJ, 640, 204
Asmus D., Hönig S. F., Gandhi P., Smette A., Duschl W. J., 2014, MNRAS, 439, 1648
Baumgartner W. H., Tueller J., Markwardt C. B., Skinner G. K., Barthelmy S., Mushotzky R. F., Evans P. A., Gehrels N., 2013, ApJS, 207, 19
Boller T., Keil R., Hasinger G., Costantini E., Fujimoto R., Anabuki N., Lehmann I., Gallo L., 2003, A&A, 411, 63
Brightman M., Nandra K., 2011, MNRAS, 413, 1206
Brightman M., et al., 2017, arXiv, arXiv:1705.10804
Bush S. J., Wang Z., Karovska M., Fazio G. G., 2008, ApJ, 688, 875-884
Downes D., Solomon P. M., Radford S. J. E., 1993, ApJ, 414, L13
Egami E., Neugebauer G., Soifer B. T., Matthews K., Becklin E. E., Ressler M. E., 2006, AJ, 131, 1253
Engel H., et al., 2010a, A&A, 524, A56
Engel H., et al., 2010b, ApJ, 724, 233
Feruglio C., Fiore F., Piconcelli E., Cicone C., Maiolino R., Davies R., Sturm E., 2013, A&A, 558, A87
Fosbury R. A. E., Wall J. V., 1979, MNRAS, 189, 79
Fried J. W., Schulz H., 1983, A&A, 118, 166
Gallimore J. F., Beswick R., 2004, AJ, 127, 239
Gerssen J., van der Marel R. P., Axon D., Mihos J. C., Hernquist L., Barnes J. E., 2004, AJ, 127, 75
Gilli R., Comastri A., Hasinger G., 2007, A&A, 463, 79
Guainazzi M., et al., 2016, MNRAS, 460, 1954
Hagiwara Y., Baan W. A., Klöckner H.-R., 2011, AJ, 142, 17
Harrison F. A., et al., 2013, ApJ, 770, 103
Harrison F. A., et al., 2016, ApJ, 831, 185
Heckman T. M., Armus L., Miley G. K., 1987, AJ, 93, 276
Hunter J. D., 2007, CSE, 9, 90
Ikebe Y., Leighly K., Tanaka Y., Nakagawa T., Terashima Y., Komossa S., 2000, MNRAS, 316, 433
Ikeda S., Awaki H., Terashima Y., 2009, ApJ, 692, 608

Iono D., et al., 2007, ApJ, 659, 283

Iwasawa K., Comastri A., 1998, MNRAS, 297, 1219

Kalberla P. M. W., Burton W. B., Hartmann D., Arnal E. M., Bajaja E., Morras R., Pöppel W. G. L., 2005, A&A, 440, 775

Komossa S., Burwitz V., Hasinger G., Predehl P., Kaastra J. S., Ikebe Y., 2003, ApJ, 582, L15

LaMassa S. M., Yaqoob T., Ptak A. F., Jia J., Heckman T. M., Gandhi P., Meg Urry C., 2014, ApJ, 787, 61

Liu Y., Li X., 2014, ApJ, 787, 52

Liu Y., Li X., 2015, MNRAS, 448, L53

Lusso E., et al., 2012, MNRAS, 425, 623

Marinucci A., et al., 2016, MNRAS, 456, L94

Max C. E., Canalizo G., Macintosh B. A., Raschke L., Whysong D., Antonucci R., Schneider G., 2005, ApJ, 621, 738

Max C. E., Canalizo G., de Vries W. H., 2007, Sci, 316, 1877

Medling A. M., et al., 2015, ApJ, 803, 61

Meijerink R., et al., 2013, ApJ, 762, L16

Mori T. I., et al., 2014, PASJ, 66, 93

Murphy K. D., Yaqoob T., 2009, MNRAS, 397, 1549

Nardini E., Risaliti G., 2011, MNRAS, 415, 619

Nardini E., Wang J., Fabbiano G., Elvis M., Pellegrini S., Risaliti G., Karovska M., Zezas A., 2013, ApJ, 765, 141

Netzer H., 2015, ARA&A, 53, 365

Netzer H., Lemze D., Kaspi S., George I. M., Turner T. J., Lutz D., Boller T., Chelouche D., 2005, ApJ, 629, 739

Noguchi K., Terashima Y., Ishino Y., Hashimoto Y., Koss M., Ueda Y., Awaki H., 2010, ApJ, 711, 144

Ohyama Y., Yoshida M., Takata T., 2003, AJ, 126, 2291

Planck Collaboration XIII, 2016, A&A, 594, A13

Ponti G., Papadakis I., Bianchi S., Guainazzi M., Matt G., Uttley P., Bonilla N. F., 2012, A&A, 542, A83

Puccetti S., et al., 2014, ApJ, 793, 26

Puccetti S., et al., 2016, A&A, 585, A157

Ricci C., et al., 2017, MNRAS, 468, 1273

Risaliti G., et al., 2006, ApJ, 637, L17

Smith R. K., Hughes J. P., 2010, ApJ, 718, 583

Soldi S., et al., 2014, A&A, 563, A57

Springel V., Di Matteo T., Hernquist L., 2005, MNRAS, 361, 776

Springel V., et al., 2005, Natur, 435, 629

Tacconi L. J., Genzel R., Tecza M., Gallimore J. F., Downes D., Scoville N. Z., 1999, ApJ, 524, 732

Tecza M., Genzel R., Tacconi L. J., Anders S., Tacconi-Garman L. E., Thatte N., 2000, ApJ, 537, 178

Treister E., Schawinski K., Urry C. M., Simmons B. D., 2012, ApJ, 758, L39

Tunnard R., Greve T. R., Garcia-Burillo S., Graciá Carpio J., Fuente A., Tacconi L., Neri R., Usero A., 2015, ApJ, 815, 114

van der Werf P. P., Genzel R., Krabbe A., Blietz M., Lutz D., Drapatz S., Ward M. J., Forbes D. A., 1993, ApJ, 405, 522

Vignati P., et al., 1999, A&A, 349, L57

Wang J., et al., 2014, ApJ, 781, 55

Wright G. S., Joseph R. D., Meikle W. P. S., 1984, Natur, 309, 430

Yaqoob T., 1997, ApJ, 479, 184

Yaqoob T., 2012, MNRAS, 423, 3360

Yaqoob T., Murphy K. D., 2011, MNRAS, 412, 277

Yoshida M., Yagi M., Ohyama Y., Komiyama Y., Kashikawa N., Tanaka H., Okamura S., 2016, ApJ, 820, 48

Yun M. S., Carilli C. L., 2002, ApJ, 568, 88